



Full Text View

[Volume 31, Issue 8 \(August 2001\)](#)

Journal of Physical Oceanography

Article: pp. 2307–2320 | [Abstract](#) | [PDF \(1.15M\)](#)

Abrupt Cooling of the Mediterranean Levantine Intermediate Water at the Beginning of the 1980s: Observational Evidence and Model Simulation

Jean-Michel Brankart^{*},¹⁰³ and Nadia Pinardi⁺

Instituto per le Scienze dell'Atmosfera e dell'Oceano, CNR, Bologna, Italy

(Manuscript received October 4, 1999, in final form November 21, 2000)

DOI: 10.1175/1520-0485(2001)031<2307:ACOTML>2.0.CO;2

ABSTRACT

The Levantine Intermediate Water (LIW) is an important water mass for the overall hydrology of the Mediterranean Sea and there are open questions connected with the possible long-term variability of its physical characteristics. This paper is dedicated to the analysis and the interpretation of the LIW long-term variations over the last 50 years. It is based on data analysis and model simulations. On the one hand, new temperature and salinity gridded data of interannual and decadal anomalies have been produced from existing historical datasets. On the other hand, a long-term primitive equation model simulation has been generated, to be compared to the observational reconstructions.

Results indicate that the major feature of both datasets (observations and model) is an intense cooling of the LIW (0.24°–0.28°C at 200-m depth) at the beginning of the 1980s (winters 1981 and 1983). Around the Aegean Sea and the Cretan Arc, the amplitude of the cooling is as large as 0.4°C.

The model simulations, forced by the Comprehensive Ocean–Atmosphere Data Set atmospheric fluxes, reproduce the cooling event quite faithfully. The possible processes at the origin of these interannual/decadal variations are discussed. Hypotheses are proposed and tested against observations. In particular it is shown that, over the period of interest, the major part of the LIW interannual/decadal variability has been directly forced by anomalies in the surface heat budget of the Eastern Mediterranean.

1. Introduction

The Mediterranean Sea has been the site of an intense and continual experimental effort during the last 30 years. Most of

Table of Contents:

- [Introduction](#)
- [Data distributions](#)
- [Interannual variability](#)
- [Model simulations](#)
- [Hypothesis on the origin](#)
- [Conclusions](#)
- [REFERENCES](#)
- [APPENDIX](#)
- [TABLES](#)
- [FIGURES](#)

Options:

- [Create Reference](#)
- [Email this Article](#)
- [Add to MyArchive](#)
- [Search AMS Glossary](#)

Search CrossRef for:

- [Articles Citing This Article](#)

Search Google Scholar for:

- [Jean-Michel Brankart](#)
- [Nadia Pinardi](#)

the water masses have been sampled sufficiently to diagnose long-term variations in their hydrological properties. This represents a unique opportunity to improve the understanding of production, transformation, and spreading of water masses and the associated forcing mechanisms.

This paper will specifically focus on a particular Mediterranean water mass, the Levantine Intermediate Water (LIW). The LIW is formed in the Levantine Basin (easternmost Mediterranean area) during winter (typically Feb or Mar) ([Wüst 1961](#); [Lascaratos et al. 1993](#)). The water then spreads westward at middepth, filling the Eastern Basin and the Tyrrhenian Sea; it is progressively transformed by mixing with surrounding water along its path toward the Western Basin ([Wu and Haines 1996](#)). The LIW corresponds to a subsurface maximum of salinity, separating deep water (colder but less salty) from surface waters. The global climatologies assign to this water a salinity (at the vertical maximum) ranging from 39.0 psu (at depth 200-m in the Levantine to 38.5 psu (at depth 500 m) in the Western Mediterranean, and a temperature ranging from 15.5°C in the Levantine to 13.5°C in the Western Mediterranean. Vertically, the LIW layer extends from 100 to 300 m in the Levantine, deepening in the Western Mediterranean to between 300 and 700 m.

Model studies have recently proved that the general circulation of the Mediterranean Sea is strongly dependent upon the temporal variability of the forcing at the air–sea interface ([Pinardi et al. 1997](#); [Korres et al. 2000](#)). Water mass formation rates are found to vary interannually ([Castellari et al. 1998](#); [Nittis and Lascaratos 1998](#)) and water mass properties can evolve on much longer timescales ([Rohling and Bryden 1992](#); [Bethoux and Gentili 1994](#)). However, until now, no comprehensive global analysis of decadal or interannual variability of the observed Mediterranean hydrology has been attempted. In this paper, we present the first objective analysis of observed T , S anomalies with respect to the climatological cycle, for the full Mediterranean area and for the period 1946–93. In parallel, a general circulation model of the Mediterranean [Modular Ocean Model (MOM): [Pacanowski et al. 1991](#)] is run for the same period, using surface atmospheric forcings from COADS (Comprehensive Ocean–Atmosphere Data Set: [da Silva et al. 1995](#)). This provides a simulated interannual dataset to be compared to the observations.


In this paper, we show that an important part of the LIW variability in the Mediterranean has occurred at interannual/decadal timescales. The changes in the LIW are found in both the model simulation and the observations. We postulate that the atmospheric interannual signal (particularly between 1981 and 1983) is mainly responsible for such changes and we carry out sensitivity experiments to show the importance of the forcing anomalies. The results confirm that the observed changes in the LIW temperature and salinity characteristics are largely connected to changes in surface heat fluxes.

In order to reach these different objectives, we will proceed in four successive steps (the four sections of the paper), proceeding from observational evidence to model simulations and interpretation. Each section is divided into several parts: the first is always dedicated to the description of the method, while the others explain the results. [Section 2](#) presents all steps of data treatment preceding the analysis. [Section 3](#) presents the statistical analysis technique used to compute the monthly T , S horizontal maps. The LIW interannual variability is studied by means of empirical orthogonal functions (EOFs). [Section 4](#) presents the primitive equation model, the long-term simulation, and the comparison of modeled versus observed variations. Finally, in [section 5](#), our hypothesis about the origin of the LIW long-term variations is described and tested.

2. Data distributions

a. Definition of interannual anomalies

In order to study interannual variability from observations, we have to compute *anomalies* with respect to the climatological cycle.

The choice of a reliable reference climatology is of fundamental importance for the analysis of anomalies. For that purpose, we have decided to compute a new version of the temperature and salinity climatology based on the new MEDATLAS historical database ([The MEDATLAS Group 1994](#)), and use the statistical analysis scheme¹ developed earlier for the Mediterranean Oceanic Data Base (MODB) dataset ([Brasseur et al. 1996](#)). In the context of this study, the main additional information contained in the MEDATLAS dataset comes from the inclusion of about 80 000 XBTs, bringing the total number of temperature profiles from 120 000 to about 200 000. [Figure 1](#)  gives an indication of the number of profiles available in some key regions of the Mediterranean (the regions represented have been selected according to their relevance for the rest of the discussion).

The statistical parameters for the objective mapping have been kept the same as those optimized for the computation of previous monthly climatologies ([Brankart and Brasseur 1996](#)). The only difference is the introduction of a Gaussian time correlation function. This modification enhances the time coherence of the solution, which becomes a monthly estimate of the climatological cycle instead of a time series of successive monthly means. The horizontal resolution of the mapping has been kept at $\frac{1}{4}^\circ$ in latitude and in longitude; all analyses are spatially bidimensional on isobaric levels.

[Figure 2](#) presents the climatology obtained for temperature at 200-m depth (annual mean). This is the depth of the LIW subsurface salinity maximum in the Eastern Mediterranean. In the rest of the paper, the detailed results will mainly be presented for this level. In [Fig. 2](#) we can recognize the well known zonal temperature gradient and the cool anomaly of the Rhodes gyre, which stands out in the Levantine Basin.

Observations at standard isobaric levels are obtained by interpolating the hydrographic profiles (when vertical resolution is judged sufficient). Data anomalies are obtained by subtracting the climatological cycle (at the corresponding standard level) interpolated (horizontally and temporally) at the profile location. This phase of data processing is based on the hypothesis that the vertical sampling of hydrographic profiles and the horizontal and temporal resolution of the climatological cycle are generally sufficient for the computation of anomalies.

b. Statistical distributions in the LIW

[Figure 3](#) presents the distribution of temperature anomalies (at depth 200 m) over the period 1946–93 in area A (all Mediterranean regions east of 10°E; see [Fig. 2](#)). This zone covers all of the Eastern Basin (comprising a major part of the Aegean and the south Adriatic Seas) together with the Tyrrhenian Sea. Averaged statistics for this area will be used throughout this paper, for discussing the data analysis results and for model intercomparison. The inclusion of the Tyrrhenian Sea is valid for studying the LIW long-term variability, even if the LIW characteristics are changing through the Strait of Sicily. In [Fig. 3](#), the large black bullets represent annual mean anomalies, computed only if the number of profiles in area A is significant. It clearly reveals an abrupt change in the anomalies distribution at the beginning of the 1980s; no other comparable change has occurred since the early 1960s. The change occurred between 1979 and 1983, followed by a slight relaxation toward warmer annual mean anomalies at the end of the 1980s.

[Figure 4](#) presents distributions of temperature anomalies at depth 200 m for two particular horizontal areas and for different time periods. [Figure 4a](#) shows the anomalies distribution over area A. [Figure 4b](#) shows the anomalies distribution in area B, a region located between 33° and 39°N, 19° and 28°E (see [Fig. 2](#)). This corresponds to the south Aegean as well as a wide zone around the Cretan Arc, extending into the Levantine and Ionian Basins. Both [Figs. 4a and 4b](#) show a set of solid curves corresponding to the anomaly distributions for two different periods, 1970–79 and 1983–92. (The distributions have been normalized in such a way that their integral is equal to one; they can thus be considered as estimates for the probability distributions of the temperature anomalies.) Each solid curve has been fitted with a Gaussian probability distribution, shown in [Fig. 4](#) by the dotted line. [Table 1](#) summarizes number of data and statistics for each of these distributions.

The difference in the distribution means for the periods 1970–79 and 1983–92 is 0.28°C for area A and 0.41°C for area B, with a 95% confidence interval of $\pm 0.01^\circ\text{C}$. [Figures 4a and 4b](#) indicate that in the period 1980–82 a major cooling has occurred, shifting the estimated decadal mean temperature by 0.28°C. [Table 1](#) also shows the mean values for the period 1946–69, which are close to the average. The period 1980–82 contains the cooling event, for which the mean values are intermediate between the warm (1970–79) and the cool (1983–92) decades. It is also clear from [Fig. 4](#) and [Table 1](#) that the cooling is largest in area B, that is, in the Aegean and Cretan Arc regions.

The asymmetry of all the distributions around their mean is evident in [Fig. 4a](#) (compare with the Gaussian curve). This is mainly due to the overabundance of extreme positive anomalies (positive tail of the distributions), which may be attributed to a larger frequency of anticyclonic eddies with positive temperature anomalies. The appearance of large negative anomalies (in area A) in the 1983–92 decade reflects the presence of cool subregions, due to inhomogeneities of the cooling inside the area (e.g., area B is part of area A, and contributes to an increase in the number of negative anomalies in the area A distribution).

Last, it is interesting to note that all the distributions of [Fig. 4](#) have a remarkably constant standard deviation (around 0.4°C; see [Table 1](#)), which means that shorter timescale variability has always been the same (in terms of total variance) during the two “decades.” The large value of this standard deviation, with respect to the 0.28°C change, is the reason why a large dataset is needed to diagnose this event. In a small dataset, it would not be easily distinguishable from small-scale noise.

3. Interannual variability from observations

a. Analysis technique

In the previous section, all data from one area and from one decade were considered equivalent and independent. They formed two homogeneous sampling sets that we used to estimate the expected mean and confidence interval of temperature variations. But data are structured in space and time and can be used to diagnose the spatial and temporal structure of interannual and decadal variability.

An objective analysis scheme has been used to estimate horizontal maps of temperature and salinity decadal/interannual anomalies at standard isobaric levels. (Details on the analysis technique are given in the appendix.) The $1^\circ \times 1^\circ$ gridded data fields have been generated for 34 isobaric levels (with a 5-m resolution between 5 and 20 m depth, 10-m resolution between 20 and 100 m, 20-m resolution between 100 and 200 m, 40-m resolution between 200 and 520 m, four levels at 580 m, 660 m, 775 m, and 925 m, and then a 300-m resolution between 1150 and 2350 m). Only decadal anomaly maps are computed below 660 m.

This new dataset contains a huge amount of information to analyze. In order to extract the dominant signals, the EOF (Lorenz 1956) technique has been used. The results are presented with all details for the 200-m level only. The solutions at depths 90 m depth and 440 m are also briefly described. For the other LIW levels, only a summary of the results is provided.

b. Main modes of temperature and salinity variations

Figure 5a shows the first EOF computed from the interannual analysis time series (yearly means) at the 200-m level. It accounts for 74% of the total variance. The second EOF (12% of variance) concerns mainly the Western Basin, while each of the remaining modes represents less than 4% of the total variance. The first mode (Fig. 5a) has been normalized in such a way that the mean over area A is equal to one. The amplitude time series (Fig. 5b, solid curve) represents, then the mean temperature variations due to that particular mode for area A. (This is also the area used to calculate the anomaly distribution of Fig. 4. This area represents the area of significant positive value in the first EOF, corresponding to a cooling when multiplied by the time series of Fig. 5b.)

The amplitude of the cooling (about 0.24°C) corresponds rather well to what has been deduced from the statistical analysis of anomaly distributions (Fig. 4). Spatially, the cooling is largest all over the LIW formation and spreading areas, together with the Aegean and the southern Adriatic Seas. The signal is weaker, but also present, in the Western Basin, especially in the Tyrrhenian Sea, in the Strait of Sicily, west of Sardinia and Corsica, and in the northernmost part (area D) where the LIW is known to propagate. A significant signal is also visible in the western Alboran Sea (area C). Later, we will describe the same signal at a deeper level, where LIW is known to be centered in the Western Mediterranean.

Figure 6 presents the same results obtained for salinity. The first EOF mode here represents about 35% of the total variance. This time, the first salinity EOF has been normalized by the mean over area A' (southern Adriatic; see Fig. 6a). Again, area A' is chosen because it is a region where the EOF takes a large value. It is a much more restricted area, covering a regional basin that works as a salt accumulator. (This is fundamental to our final interpretation of the cooling event.) The correlation between temperature and salinity amplitude time series for the first mode (Figs. 5b and 6b) is more than 80%. The temperature change of the early 1980s is accompanied by a salinity change: salinity increase in the southern Adriatic, in the north Aegean, and in the Alboran Sea. In the rest of the Eastern Basin the mode indicates a small salinity decrease. A word of caution should be given in interpreting this small salinity decrease since the data distribution is poor and the EOF values are small.

In Fig. 7 we have plotted, as a function of depth, the difference between the temperature and the salinity between the two decades already used as reference in section 2 (1970–79 and 1983–92), averaged over the different areas indicated in Figs. 5a and 6a. (The averages are now computed from the gridded data, not from the original observations.) Globally, we can say that the maximum amplitude of the cooling is around 200–300 m in the Eastern Basin, while it is deeper in the Western Mediterranean, around 500 m, as expected since the LIW is deeper there. The behavior of the salinity is much more complex, showing in the 1980s an increase at all depths and for all areas except the surface in area B'.

Since the temperature anomaly (Fig. 7) shows a depth range for the event between 50 and 500 m, we are going to give more details on how the structure of the cooling event varies with depth. First, between 90- and 440 m depth, the first EOF of the interannual and decadal analysis time series of temperature is always characteristic of the 1981–83 change, and it always represents more than 50% of the total variance. (It is still present at shallower levels in the Eastern Mediterranean, and at deeper levels in the Western Mediterranean, but other signals are becoming important.) In Fig. 8, we show the first EOF at depth 90 m (51% of the total variance; Fig. 8a) and at 440-m (52% of the total variance; Fig. 8b). (They are still normalized in such a way that the mean over area A is equal to one, as in Fig. 5a). From these figures, we observe that in the shallow levels (depth 90-m), the dominant signal is in the Eastern Mediterranean, while in the deep levels (depth 440 m) the most intense cooling takes place in the Western Mediterranean (as already observed in Fig. 7). In Fig. 8c, we show the corresponding time series (corresponding to the mean over area A, as in Fig. 5b). When the depth increases, the high frequency variations are progressively filtered out so that the time series become smoother. Moreover, at depth 440 m, the signal maximum has not only moved westward, but the cooling is also somewhat delayed. This may be interpreted as indicating that cooling at this depth does not come directly from the surface but laterally, from the cooler LIW waters of the Strait of Sicily.

In conclusion, we refer to the observed cooling event as a decadal/interannual variability signal since 1) it occurred over a

short time period and 2) the decadal mean temperature shifted about 0.24–0.28°C across 1981–83 (at depth 200 m). This kind of event can occur in larger ocean basins, such as in the Pacific in the 1970s (Miller et al. 1994). The question to be answered now is: can we simulate the decadal/interannual change in temperature? If yes, can we explain such change in terms of atmospheric forcing variability? The next sections are devoted to the analysis of the model results.

4. Model simulations

a. Model design

The interannual variability of the Mediterranean general circulation has been simulated using the MOM implemented for the Mediterranean Sea. This is a rigid-lid primitive equation model, using a streamfunction formulation to solve for the barotropic mode. The horizontal friction and diffusion coefficients have been kept small compared with others studies (Rousset et al. 1995; Haines and Wu 1998; Korres et al. 2000): we use 8×10^{18} and $3 \times 10^{18} \text{ cm}^4 \text{ s}^{-1}$, respectively. In the vertical, we have used constant vertical viscosity and diffusivity (1.5 and $0.3 \text{ cm}^2 \text{ s}^{-1}$, respectively), with convective adjustment in case of vertical instability. [In more specific studies, Wu and Haines (1996, 1998) have used even lower viscosity and diffusivity coefficients. In the second paper, they have also tested a vertically variable mixing scheme.] The model grid has 31 levels in the vertical and the horizontal resolution is $1/4^\circ$ in latitude and longitude. West of the Strait of Gibraltar, we use a box of Atlantic water (about $3^\circ \times 3^\circ$), where temperature and salinity are relaxed to climatology. [See Korres et al. (2000) for more details about the model.]

In order to carry out such a long-term interannual simulation we have chosen to force the model with monthly mean surface fluxes (wind stress and heat flux) directly diagnosed from COADS data (da Silva et al. 1995). This dataset extends from 1945 to 1993. The horizontal resolution is 1° . Because of the lack of any accurate dataset for the interannual variability of freshwater fluxes (evaporation, precipitation, river runoff), sea surface salinity is relaxed to monthly mean climatology, with a relaxation period of 5 days.

However, if the COADS heat flux was imposed without any feedback from the predicted sea surface temperature, a strong drift in the mean volume temperature would result, leading progressively to unphysical situations. The COADS net mean heat flux over the 49 years is indeed about 10 W m^{-2} , while it is known that the long-term Mediterranean surface heat budget should be negative (about -7 W m^{-2} ; Castellari et al. 1998). Thus, we had to apply a correction that is specified as follows:

$$Q_t = Q_t^* - \left(\frac{\partial Q_t}{\partial T} \right)_{T=T^*} (T - T^*), \quad (1)$$

where T^* and Q_t^* are the monthly mean interannual surface temperatures and heat fluxes from COADS, T is the temperature predicted by the model, and Q_t the actual heat flux applied to the model. As an estimation of the term $\partial Q_t / \partial T$, we used a constant value computed from bulk formulations, using typical values for the Mediterranean:

$$\left(\frac{\partial Q_t}{\partial T} \right)_{T=T^*} = 25 \text{ W m}^{-2} \text{ K}^{-1}. \quad (2)$$

Using that formulation, we obtain a long-term climatological mean value of about -4 W m^{-2} , which is compatible with the available data. This means that the given COADS surface fluxes are not compatible with sea surface temperatures (T^*), and our correction modifies the heat flux so as to be more consistent with those values. The Q_T and Q_T^* time series are shown in Fig. 9a. We notice that the interannual variability has been decreased to about 5 W m^{-2} from about 10 W m^{-2} , which had been already disputed as being unrealistic by Garrett et al. (1993) for another COADS heat flux dataset.

Figure 9b represents the Q_T and Q_T^* mean winter heat flux interannual anomalies averaged over area A (see Fig. 5a). We remark that the two lowest values of the 49-yr time series are in 1981 and 1983, the years of the LIW cooling found in the previous section.

b. Comparison with observations

Using the forcing presented above, we have been able to produce a 48-yr interannual simulation, without significant drift

of the volume mean temperature. We can now extract the LIW simulated variability and carry out the same analysis that was done on the statistically interpolated data.

The model-predicted yearly mean temperature fields at 200 m have been projected onto the first EOF mode obtained from the observations (Fig. 5a). The resulting amplitude time series is shown in Fig. 10. The model has been able to reproduce the amplitude of the LIW cooling in the years 1980–83. The correlation between the data and model time series of Fig. 10 reaches 69%, and even 82% if we remove what comes before 1960. Thus, the first conclusion is that the decadal/interannual variability of the surface heat flux forcing is capable of driving some of the observed temperature changes in the LIW layer. By this we mean that decadal changes can occur in a very short timescale due to atmospheric anomalies, as also shown by Miller et al. (1994) for the North Pacific area.

c. Sensitivity experiment

A mathematical or numerical model is always an idealization and simplification of the complex natural system. It is therefore difficult, when good agreement is obtained between simulations and observations, to be sure that the right physical processes have been considered and correctly simulated.

Our model ignores the freshwater flux that effectively controls the sea surface salinity. Would it then be possible that interannual variations of the freshwater balance has played an important role in driving LIW interannual temperature variations? Is it possible that, in the model simulation, the cooling of the LIW has been only controlled by surface heat flux, while, in reality, it would have also required a modification of surface salinity?

A first test on the model simulation is performed by modifying the forcing fields in such a way as to eliminate the 1981 and 1983 winter (Jan–Mar) cooling event. For that purpose, the heat flux applied to the model has been changed to the climatology on area A (see definition in Fig. 5a) for the winters 1980–83 (Fig. 9b). The simulated temperature changes are shown by the dotted curve plotted in Fig. 10. The cooling event has almost totally disappeared for that period. It consequently becomes clear that, for this model, the cooling is a direct consequence of the extreme winter heat flux observed in 1981 and 1983. Nevertheless, the very low decadal mean heat flux of the 1980s (Fig. 9a) still produces a decadal decrease in temperature, which brings the simulated and observed temperatures together at the end of the 1980s.

5. Hypothesis on the origin of LIW interannual changes

a. Formulation of the hypothesis

In this section, we would like to test explicitly the hypothesis that interannual variations in the winter heat flux provide the dominant contribution to the LIW temperature changes found in the observations. Then, using that hypothesis, we will diagnose some quantitative properties of the LIW renewal process (renewal time and its dependence on heat flux anomaly). To do this, we will develop a simple model for the LIW temperature changes, explicitly make the hypothesis of the importance of the heat flux, and attempt to fit the model to observations. The skill of the fit will indicate the validity of our assumptions. Conversely, if interannual variations in the freshwater balance become significant, the model fit to observations will be poor.

Let us consider a very simple model for the LIW mean temperature *interannual anomaly* (T_{LIW}) at some depth:

$$\frac{dT_{\text{LIW}}}{dt} = \frac{1}{\tau}(T_F - T_{\text{LIW}}), \quad (3)$$

where τ is the LIW renewal time, T_{LIW} is the LIW temperature, and T_F is the surface temperature at formation time. Both T_{LIW} and T_F are anomalies with respect to LIW mean climatic temperature at the depth of interest. In practice, we will ignore seasonality and approximate (3) by a discrete model, only considering year-to-year changes.

In general, the formation rate cannot be supposed constant. It depends on the quantity of surface water that reaches the critical density, in order to permit convection down to LIW depths. Nor can T_F be supposed constant. At interannual timescale, these variables can be related to three quite independent factors: heat flux, freshwater flux, and circulation preconditioning. Here, we make the hypothesis that, with respect to LIW, the heat flux is the dominant factor.

We assume a linear relation between the mean winter heat flux anomaly (Q_w) and the surface formation temperature anomaly T_F (water formation usually takes place at the end of winter), with a the constant of proportionality:

$$T_F = \alpha Q_t. \quad (4)$$

At this point, only the formation rate (τ) remains to be modeled. A first possibility would be to treat it as constant. But we would like to test the importance of formation rate variations as a function of Q_t : we know indeed that the formation rate will be higher during cool atmospheric winters and lower during warm atmospheric winters. We look for a formulation that breaks the symmetry between positive and negative heat flux anomalies. One possibility is to evaluate the proportion of surface water susceptible to convection, which depends on the density distributions at the surface and at the LIW level. If the distributions are supposed Gaussian, the hypothesis of the heat flux as a dominant factor leads to

$$\frac{1}{\tau} = \frac{2}{\tau_0} \operatorname{erf}\left(\frac{T_{\text{LIW}} - T_F}{\sigma}\right), \quad (5)$$

where σ is a standard deviation that takes into account the spatial variations of water masses (salinity as well as temperature, at the surface and at the subsurface LIW layer). From this relation, τ_0 is the formation rate at equilibrium ($T_{\text{LIW}} = T_F$).

As written, this simple model is controlled by three parameters (τ_0 , α , σ) and one forcing function (Q_T). If we suppose the formation rate to be constant, the model becomes much simpler (linear) with only two parameters, τ_0 and α .

b. Estimation of parameters

This simple model, however, would be impossible to solve in a predictive mode since the parameters are unknown, and we would like to take into account possible error on the forcing. The parameters are found by minimizing the cost function:

$$J = \frac{1}{2\Delta t} \int \frac{1}{\sigma_T^2} (T_{\text{LIW}} - T_{\text{LIW}}^*)^2 dt + \frac{1}{2\Delta t} \int \frac{1}{\sigma_Q^2} (Q_t - Q_t^*)^2 dt, \quad (6)$$

where Δt is the period of the simulation, T_{LIW}^* is the observed LIW temperature (Fig. 11a) and Q_T^* is the observed COADS heat flux (Fig. 11b), both averaged over area A. This problem is combined with the strong constraint that T_{LIW} is a solution of Eq. (3). In practice, this minimization problem is solved using a steepest descent algorithm. The gradient of the cost function with respect to the control parameters is computed using the adjoint of the linear tangent model.

Errors on LIW mean temperature are represented by σ_T in (6). They are directly deduced from the mapping error statistics. On the other hand, analyses of the sensitivity of Q_T to various bulk formulation and to various meteorological datasets leads to an estimate of $\sigma_Q = 10 \text{ W m}^{-2}$ (Castellari et al. 1998).

c. Test of the hypothesis

Results are presented for the two versions of the model with two (τ_0 and α) and three (τ_0 , α , and σ) physical parameters, respectively. The solutions obtained are shown in Fig. 11a. The associated corrected heat fluxes are represented in Fig. 11b. The minimum values of the cost function are $J = 0.94$ for the two-parameter model and $J = 0.76$ for the three-parameter model. Values lower than 1 mean that the difference between observed and diagnosed values are clearly below the prior error estimations. Thus, the observations do not falsify our hypotheses. According to our simple model, the interannual heat balance variations are capable of explaining the interannual variability of the LIW.

The values that are diagnosed for the parameters τ_0 and α are

$$\tau_0 = 3.4 \text{ yr}, \quad \alpha = 0.0088^\circ\text{C}(\text{W m}^{-2})^{-1} \quad (7)$$

for the two-parameter model, and

$$\tau_0 = 2.7 \text{ yr}, \quad \alpha = 0.0058^\circ\text{C}(\text{W m}^{-2})^{-1} \quad (8)$$

for the three-parameter model. In the latter case, the optimal value for σ is 5.4°C . However, since the solution is not very sensitive to values of σ between 2.5° and 7°C , the significance of this value remains problematic. The values obtained for τ_0 mean that for the overall area A, a renewal time of 2.5–3.5 yr is consistent with the interannual temperature changes.

In order to understand the effect of the asymmetry introduced by (5), let us compare the results of the two models with and without that formulation. In Fig. 11b, we can see that the two-parameter model leads to underestimation of the positive heat flux anomalies (especially during the later 1970s, when the T_{LIW} observational time series is most reliable). With a constant renewal time (as in the two-parameter model), these positive heat flux anomalies would lead to unrealistic heating of LIW, unless the heat flux is changed considerably. It is interesting to note that the three-parameter model leads to a modified renewal time as long as 4.2 yr for anomalies of $+30 \text{ W m}^{-2}$ (such as in 1979), and as short as 1.7 yr for anomalies of -50 W m^{-2} (such as 1983).

Finally, we would like to speculate about the salinity variations shown in Fig. 6b. Globally, in the Levantine as well as in the Ionian Basins, the data show that the salinity has at most slightly decreased (during the change in the 1980s, together with the temperature decrease). On the contrary, in the peripheral area, such as the south Adriatic, the north Aegean and the Alboran Seas, salinity has strongly increased. We may then argue that these regional salinity changes are consequences of the main heat flux event of 1981–83, which caused an increase in the formation rate of LIW. Thus, it may be possible that a larger quantity of LIW has been advected into these lateral areas, locally increasing the salinity. Our hypothesis is that the behavior of salinity variations in the LIW would be indirectly driven by surface heat flux fluctuations through an enhanced redistribution process. Similar processes have been found to occur in the Aegean (Wu et al. 2000) and have triggered deep-water formation and overflow from the Aegean straits.

6. Conclusions

The goal of this work is the accurate reconstruction of the LIW long-term variations from observations and numerical simulations. We have tried to understand this problem from several points of view (global statistical characteristics, objective mapping, general circulation model, and process studies) and to associate levels of confidence with the different types of results that have been produced.

According to our study, an abrupt cooling of LIW occurred at the beginning of the 1980s (0.24° – 0.28°C on average depth at 200 m). Observations have been sufficient to resolve the spatial structure of the cooling change, which shows a maximum intensity in the Cretan Arc region (the starting area of the phenomenon). A long-term simulation, forced with COADS interannual heat flux anomalies, reproduces quite adequately the observed evolution. Moreover, we tested the conjecture that the observed change is a direct consequence of 1981–83 heat flux anomalies found in the 49 years of the COADS time series. Shorter term LIW variability was also found to be generated by atmospheric forcing by Nittis and Lascaratos (1998). Moreover, our study has shown the largest-scale change in LIW characteristics ever found. The site of its occurrence is also shifted with respect to the Rhodes gyre region, and it is centered in the southern Aegean, as also found by Roether et al. (1997).

Before concluding, we would like to mention two other studies of long-term Mediterranean water mass variations. The first, by Bethoux et al. (1990), concerns a continuous increase of the Western Mediterranean deep water temperature since the early 1960s. The second one, by Roether et al. (1996), concerns a sudden modification of the Eastern Mediterranean deep waters between 1987 and 1995 starting from the Aegean Sea. These phenomena concern denser, cooler, but less saline water and are only indirectly linked to LIW formation process. However, it is possible that both vertical and horizontal redistribution processes, which we have shown here to be associated with anomalous heat fluxes, could be responsible for all these different water mass changes.

The observations used in this paper show that, in the Mediterranean, LIW changes occur at interannual and decadal timescales. Our data also support the idea that significant deep ocean variations can be forced by regional atmospheric anomalies or extreme situations. In other words, a regional atmospheric anomaly can produce a global water mass change at intermediate depth.

Acknowledgments

This work has been supported by the EU-MAST programme (Contract MAS3-CT96-5019) and the MATER-MTP-II project (MAS3-CT96-0051). We would like to thank the MEDATLAS project for providing the data and the MODB project

REFERENCES

- Bethoux J., and B. Gentili, 1994: The Mediterranean Sea, a test area for marine and climatic interaction. *Ocean Processes in Climate Dynamics: Global and Mediterranean Examples*, P. Malanotte-Rizzoli and A. Robinson, Eds., NATO ASI Series, Vol. 419, Kluwer Academic, 239–254.
- Bethoux J., B. Gentili, and D. Tailliez, 1990: Warming trend in the Western Mediterranean deep water. *Nature*, **347**, 660–662. [Find this article online](#)
- Brankart J.-M., and P. Brasseur, 1996: The general circulation in the Mediterranean Sea: A climatological approach. *J. Mar. Syst.*, **18**, 41–70. [Find this article online](#)
- Brasseur P., 1991: A variation inverse method for the reconstruction of general circulation fields in the northern Bering Sea. *J. Geophys. Res.*, **96**, 4891–4907, (C3),.
- Brasseur P., J.-M. Beckers, J.-M. Brankart, and R. Schoenauen, 1996: Seasonal temperature and salinity fields in the Mediterranean Sea: Climatological analyses of an historical data set. *Deep-Sea Res.*, **43**(2,), 159–192.
- Bretherton F. P., R. E. Davis, and C. B. Fandry, 1976: A technique for objective analysis and design of oceanographic experiment applied to MODE-73. *Deep-Sea Res.*, **23**, 559–582.
- Castellari S., N. Pinardi, and K. Leaman, 1998: A model study of air–sea interactions in the Mediterranean Sea. *J. Mar. Syst.*, **18**, 89–114. [Find this article online](#)
- da Silva A. M., C. C. Young, and S. Levitus, 1995: *Atlas of Surface Marine Data 1994*. Vol 1: *Algorithms and Procedures*. NOAA Atlas NESDIS 7, 78 pp.
- Gandin L. S., 1965: *Objective Analysis of Meteorological Fields*. Israel Program for Scientific Translation, 242 pp.
- Garrett C., R. Outerbridge, and K. Thompson, 1993: Interannual variability in Mediterranean heat and buoyancy fluxes. *J. Climate*, **6**, 900–910. [Find this article online](#)
- Haines K., and P. Wu, 1998: GCM studies of intermediate and deep waters in the Mediterranean. *J. Mar. Syst.*, **18**, 197–214. [Find this article online](#)
- Korres G., N. Pinardi, and A. Lascaratos, 2000: The ocean response to low-frequency interannual atmospheric variability in the Mediterranean Sea. Part I: Sensitivity experiments and energy analysis. *J. Climate*, **13**, 705–731. [Find this article online](#)
- Lascaratos A., R. Williams, and E. Tragou, 1993: A mixed layer study of the formation of Levantine Intermediate Water. *J. Geophys. Res.*, **98**, 14 739–14 749, (C8),.
- Lorenz E., 1956: Empirical orthogonal functions and statistical weather prediction. Department of Meteorology, Massachusetts Institute of Technology Statistical Forecast Project Rep. 1, 27 pp.
- The MEDATLAS Group., 1994: Specifications for the Mediterranean data banking. Tech. Rep., Sismer-Ifremer, Brest, France, 28 pp.
- Miller A., D. Cayan, T. Barnett, N. Graham, and J. Oberhuber, 1994:: The 1976–77 climate shift of the Pacific Ocean. *Oceanography*, **7**, 21–26. [Find this article online](#)
- Nittis K., and A. Lascaratos, 1998: Diagnostic and prognostic numerical studies of LIW formation. *J. Mar. Syst.*, **18**, 179–195. [Find this article online](#)
- Pacanowski R., K. Dixon, and A. Rosati, 1991: Readme file for GFDL MOM 1.0. GFDL–NOAA Tech. Rep.
- Pinardi N., G. Korres, A. Lascaratos, V. Roussenov, and E. Stanev, 1997: On the interannual variability of the Mediterranean Sea upper ocean circulation. *Geophys. Res. Lett.*, **24**, 425–428. [Find this article online](#)
- Roether W., B. Manca, B. Klein, D. Bregant, D. Georgopoulos, V. Beitzel, V. Kovacevic, and A. Luchetta, 1996: Recent changes in Eastern Mediterranean deep waters. *Science*, **271**, 333–335. [Find this article online](#)
- Roether W., B. Klein, V. Beitzel, and B. Manca, 1997: Property distributions and transient-tracer ages in Levantine Intermediate Water in

the Eastern Mediterranean. *J. Mar. Syst.*, **18**, 71–87. [Find this article online](#)

Rohling E. J., and H. L. Bryden, 1992: Man-induced salinity and temperature increases in Western Mediterranean Deep Water. *J. Geophys. Res.*, **97**, 11 191–11 198, (C7),.

Roussenov V., E. Stanev, V. Artale, and N. Pinardi, 1995: A seasonal model of the Mediterranean Sea. *J. Geophys. Res.*, **100**, 13 515–13 538.

Wahba G., and J. Wendelberger, 1980: Some new mathematical methods for variational objective analysis using splines and cross validation. *Mon. Wea. Rev.*, **108**, 1122–1143. [Find this article online](#)

Wu P., and K. Haines, 1996: Modelling the dispersal of Levantine Intermediate Water and its role in Mediterranean deep water formation. *J. Geophys. Res.*, **101**, 6591–6607, (C3),.

Wu P., and K. Haines, 1998: The general circulation of the Mediterranean Sea from a 100-year simulation. *J. Geophys. Res.*, **103**, 1121–1135, (C1),.

Wu P., K. Haines, and N. Pinardi, 2000: Toward an understanding of deep-water renewal in the Eastern Mediterranean. *J. Phys. Oceanogr.*, **30**, 443–458. [Find this article online](#)

Wüst G., 1961: On the vertical circulation of the Mediterranean Sea. *J. Geophys. Res.*, **66**, 3261–3271.

APPENDIX

7. The Statistical Analysis Scheme

Statistical analysis methods (based on the Gauss–Markov theorem) have been widely used in meteorology and oceanography ([Gandin 1965](#); [Bretherton et al. 1976](#)) to grid unevenly spaced data. From a set of sparse data anomalies (with respect to a prior background), these methods provide the local expected value of the signal with minimum expected error. In our case, we use the climatological cycle as a background and analyze data anomalies (see [section 3](#)). The objective analysis procedure requires a knowledge of the data and background error covariances (supposed unbiased), which we will specify in the following discussion.

Our problem is characterized by a huge amount of data to be analyzed simultaneously, and which does not require a very complex statistical model (e.g., the energy of the signal is mainly in the large scales, and the noise may be supposed fully random) so that the spline variational formulation can be used ([Wahba and Wendelberger 1980](#)). This method is very scale selective and can be effectively used as an adjustable low-pass filter. Our scope is to reconstruct regularly gridded fields whose spectral content is as homogeneous as possible; this leads to postulate homogeneity and isotropy of the statistical model (for background error as well as for data error), even if, in certain locations, data density would be sufficient to resolve smaller structures. As such, the procedure is then completely controlled by the signal to noise ratio and the signal correlation function (in space and time).

[Table A1](#) summarizes the parameters of the statistical model that have been used for interannual and decadal analysis of temperature and salinity anomalies at depth 200 m. Correlation timescales have been computed in order to perform interannual or decadal analysis (assuming that these timescales contain a significant and important part of the basin variability). Horizontal correlation lengths have been selected according to what we can reasonably expect to resolve at decadal and interannual timescales from the quantity of data available. In both cases we expect that a significant part of the interannual or decadal variance is present at very large horizontal scales. A reasonable choice with respect to the data distribution is that, if we resolve shorter timescales, we lose resolution on the spatial structure, and vice versa. These scales limit the portion of the power spectrum resolved; they dictate the separation between signal and noise variances from the total data variance.

A very simple procedure has been applied to estimate the signal to noise ratio. We form an ensemble of horizontal and temporal boxes, dimensioned according to horizontal and temporal correlation scales (i.e., if the distance between two observations is smaller than the correlation length scale or timescale, they can be put inside the same box). The noise variance is then the observation variance inside each box and the signal variance is the variance of the box-averaged values. The decadal and interannual signals, as they have been defined for this analysis, represent between 5% and 15% of total data variance (see [Table A1](#)). These low variance values depend on our choice of resolved horizontal scales as shown in [Table A1](#). We also notice that most of the variance at the decadal timescales comes from the LIW cooling during the 1980s. Sensitivity analysis of the signal to noise ratio (from 1% to 40%) does not exhibit any quantitative change in the amplitude of the cooling; only the spatial structures become either excessively smooth or excessively rough compared with the selected correlation scales.

In practice, the spline variational problem is solved using a finite element technique (Brasseur 1991). The main advantage is a numerical cost almost independent of the number of data analyzed, while the only approximation lies in the representation of the (continuous) solution. The mesh that has been used allows us to resolve horizontal scales well below the limit of the low-pass filter defined in Table A1. Finite elements also permit us to easily take into account the complex basin geometry, by *automatically* prohibiting correlations across land barriers. This is especially important in our analyses, which are characterized by large horizontal scales, comparable with the size of coastal irregularities (see solution in Figs. 5 and 6). Maps of error estimates are also computed, taking into account the same technical advantages (Brankart and Brasseur 1996). They will be used to provide confidence intervals for the analysis results.

The finite element technique is especially efficient for 2D problems. For that reason, the time coordinate has been treated separately: a 2D horizontal analysis problem is solved at any time for which the analysis is required (monthly or yearly depending on time correlation). All data available are systematically used, modifying only the observation error standard deviation according to the difference (Δt) between analysis time and observation time:

$$\sigma_*^2 = \frac{1}{\gamma(\Delta t)}(\sigma^2 + \epsilon^2) - \epsilon^2, \quad \gamma(\Delta t) = \exp\left(-\frac{\Delta t^2}{T^2}\right), \quad (\text{A1})$$

where σ and ϵ are data and background error standard deviations, γ is the temporal correlation function, and T is the correlation timescale (see Table A1). This relation has been established in order to conserve the diagonal of the data covariance matrix equivalent to the 3D problem.

This fully defines the analysis method, developed especially for its ability to take into account, *simultaneously*, a huge set of observations at their exact horizontal and temporal locations, without any data aggregation or data selection. This point is of fundamental importance, especially when dealing with large noise-to signal ratio or large correlation scales, which necessitate a high level of data redundancy. For further processing, the solution has then been sampled onto a regular horizontal grid of $1^\circ \times 1^\circ$, every month for the period 1946–93.

Tables

TABLE 1. Number of data, mean, and standard deviations of different subsets of temperature data anomalies at depth 200 m. Subsets are organized according to the period and according to the horizontal area (A and B). Figures between parentheses represent statistics for the Gaussian distribution fitted to the experimental data distribution

	Area A	Area B
Number of data		
1946–69	11 659	3364
1970–79	24 873	10 168
1980–82	4175	1179
1983–92	19 132	4857
Mean of the distributions		
1946–69	+0.038 (+0.002)	+0.037 (+0.000)
1970–79	+0.124 (+0.078)	+0.139 (+0.095)
1980–82	-0.083 (-0.091)	-0.134 (-0.125)
1983–92	-0.154 (-0.162)	-0.262 (-0.296)
Standard deviations		
1946–69	0.403 (0.335)	0.439 (0.384)
1970–79	0.391 (0.330)	0.411 (0.351)
1980–82	0.370 (0.310)	0.378 (0.318)
1983–92	0.399 (0.311)	0.485 (0.362)

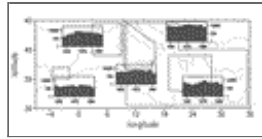
[Click on thumbnail for full-sized image.](#)

TABLE A1. Summary of the statistical parameters that have been used for interannual and decadal analysis in the LIW (at depth 200 m)



	Temperature		Salinity decadal variability
	Decadal variability	Interannual variability	
Correlation timescale	10 years	6 months	10 years
Horizontal correlation length	800 km	1200 km	800 km
Total observation standard deviation	0.52°C	0.52°C	0.130 psu
Signal standard deviation	0.12°C	0.17°C	0.031 psu
Noise standard deviation	0.50°C	0.49°C	0.126 psu
Signal to noise variance ratio	5.5%	12.0%	5.3%

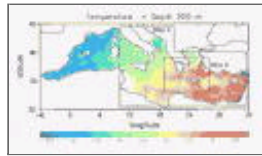
[Click on thumbnail for full-sized image.](#)

Figures



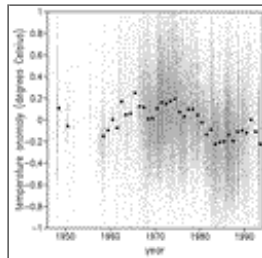
[Click on thumbnail for full-sized image.](#)

FIG. 1. Time distributions (5-yr groups) of the profiles available in the MEDATLAS database, for some key regions of the Mediterranean. The regions are shown by the dashed polygons. Distributions are for (top left) the Ligurian-Provençal Basin, (bottom left) the Alboran Sea, (middle) the Tyrrhenian Sea, (top right) the Eastern Mediterranean together with the Tyrrhenian Sea (area A of [Fig. 2](#) ) , and (bottom right) the Cretan Arc region (area B of [Fig. 2](#) )



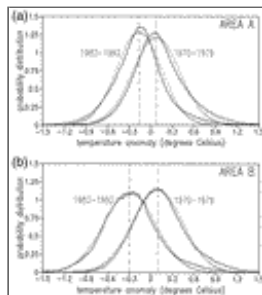
[Click on thumbnail for full-sized image.](#)

FIG. 2. Annual mean climatology for temperature at depth 200 m ($^{\circ}\text{C}$). Areas A and B are shown by the polygons



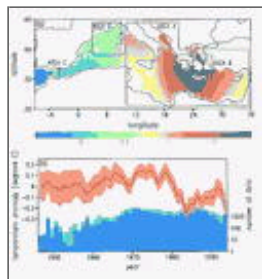
[Click on thumbnail for full-sized image.](#)

FIG. 3. Temporal distributions of temperature data anomalies ($^{\circ}\text{C}$). For area A, at depth 200 m. Bullets represent annual means



[Click on thumbnail for full-sized image.](#)

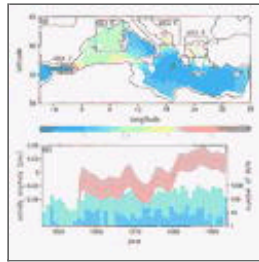
FIG. 4. Normalized distributions of temperature anomalies ($^{\circ}\text{C}$) at depth 200 m for (a) area A and (b) area B. Solid curves are normalized data distributions and dotted curves are corresponding fitted Gaussians. The two periods are 1970–79 and 1983–92



[Click on thumbnail for full-sized image.](#)

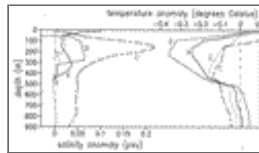
FIG. 5. (a) First EOF of temperature interannual variability at depth 200 m (74% of total variance). The mode has been normalized such that the mean over area A is 1. (b) The associated amplitude time series (red curve) represents temperature variations ($^{\circ}\text{C}$) averaged over area A, due to that first EOF mode. The orange zone is the 95% confidence interval. The light blue histogram is the

yearly data distribution for the whole Mediterranean Sea, while the darker blue gives the number of data in area A



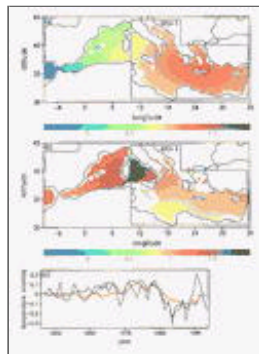
Click on thumbnail for full-sized image.

FIG. 6. (a) First EOF of salinity interannual variability at depth 200 m (35% of total variance). The mode has been normalized such that the mean over area A' is 1. The location of areas A', B', C', and D' are indicated by the polygons. (b) The associated amplitude time series (red curve) represents the salinity variations (psu), averaged over area A', due to that particular mode. The orange zone is the 95% confidence interval. The light blue histogram is the yearly data distribution for the entire Mediterranean Sea, while the darker blue gives the number of the data in area A'



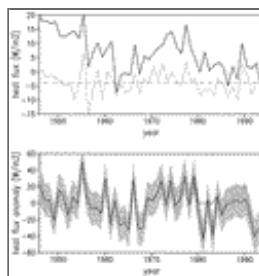
Click on thumbnail for full-sized image.

FIG. 7. Amplitude of the cooling (right: in °C) and of the salinity change (left: in psu), between the 1970s (1970–79) and the 1980s (1983–92), presented as functions of depth. The different profiles refer to the zones defined in [Figs. 5a and 6a](#), for temperature and salinity, respectively



Click on thumbnail for full-sized image.

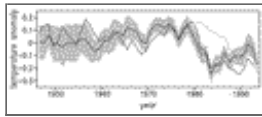
FIG. 8. (a) First EOF of temperature interannual variability at depth 90 m (51% of total variance). The mode has been normalized such that the mean over area A is 1. (b) First EOF of temperature interannual variability depth at 440 m (51% of total variance). The mode has been normalized such that the mean over area A is 1. (c) The associated amplitude time series represents temperature variations (°C) averaged over area A due to the first EOF modes for the three depths: 90 m (blue curve), 200 m (black curve), and 440 m (red curve)






Click on thumbnail for full-sized image.

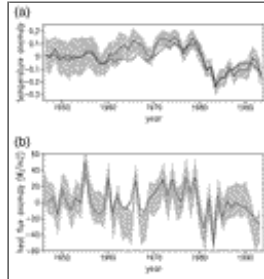
FIG. 9. (a) Annual mean values of surface averaged heat flux from plain COADS value ([da Silva et al. 1995](#)) Q_t^* (plain curve), and with flux correction [[Eq. \(2\)](#)] Q_t (dotted curve). The horizontal dashed line represents the corrected flux average value (about -4 W m^{-2}). (b) Mean winter heat flux interannual anomalies for Q_t and Q_t^* (W m^{-2}) averaged over area A. The solid curve stands for COADS data, Q_t^* , and the dotted curve stands for the fluxes corrected with [Eq. \(2\)](#), Q_t . The dashed curve represents the

modified heat fluxes used for the sensitivity experiment. The shaded area is the 95% confidence interval




[Click on thumbnail for full-sized image.](#)

FIG. 10. Temperature anomaly time series (dashed curve: in °C) resulting from the projection of the yearly mean simulated field at 200 m on the data first EOF mode of [Fig. 5a](#) . The observed data time series (solid curve) is repeated from [Fig. 5b](#) . The dotted curve is the result of a sensitivity experiment using a modified heat flux on the period 1980–83 (dashed curve of [Fig. 9b](#) ). The shaded area is the 95% confidence interval



[Click on thumbnail for full-sized image.](#)

FIG. 11. (a) Area A mean temperature anomalies (dashed and dotted curves: °C), estimated by solving the minimization problem in [Eq. \(6\)](#). The data time series (solid curve) is repeated from [Fig. 5b](#)  for comparison. (b) Mean winter heat flux interannual anomaly (W m^{-2}) averaged over area A, as estimated by minimizing the functional in [Eq. \(6\)](#). The dotted curve is the time series obtained with the two-parameter model and the dashed curve is the time series obtained with the three-parameter model

¹ In that way, the same dataset and the same analysis method are used for the estimation of the climatology and for the analysis of interannual anomalies (see [section 3](#)).

* Current affiliation: MEOM-LEGI, Grenoble, France.

+ Current affiliation: Corso di Scienze Ambientali, Bologna University, Ravenna, Italy.

Corresponding author address: Dr. Jean-Michel Brankart, MEOM-LEGI, B.P. 53X, F-38041 Grenoble Cedex, France. E-mail: jean-michel.brankart@hmg.inpg.fr

[top](#) ▲

